Volume 1 | Number 4 | April 2019 | Pages 1263–1610

Nanoscale Advances

rsc.li/nanoscale-advances

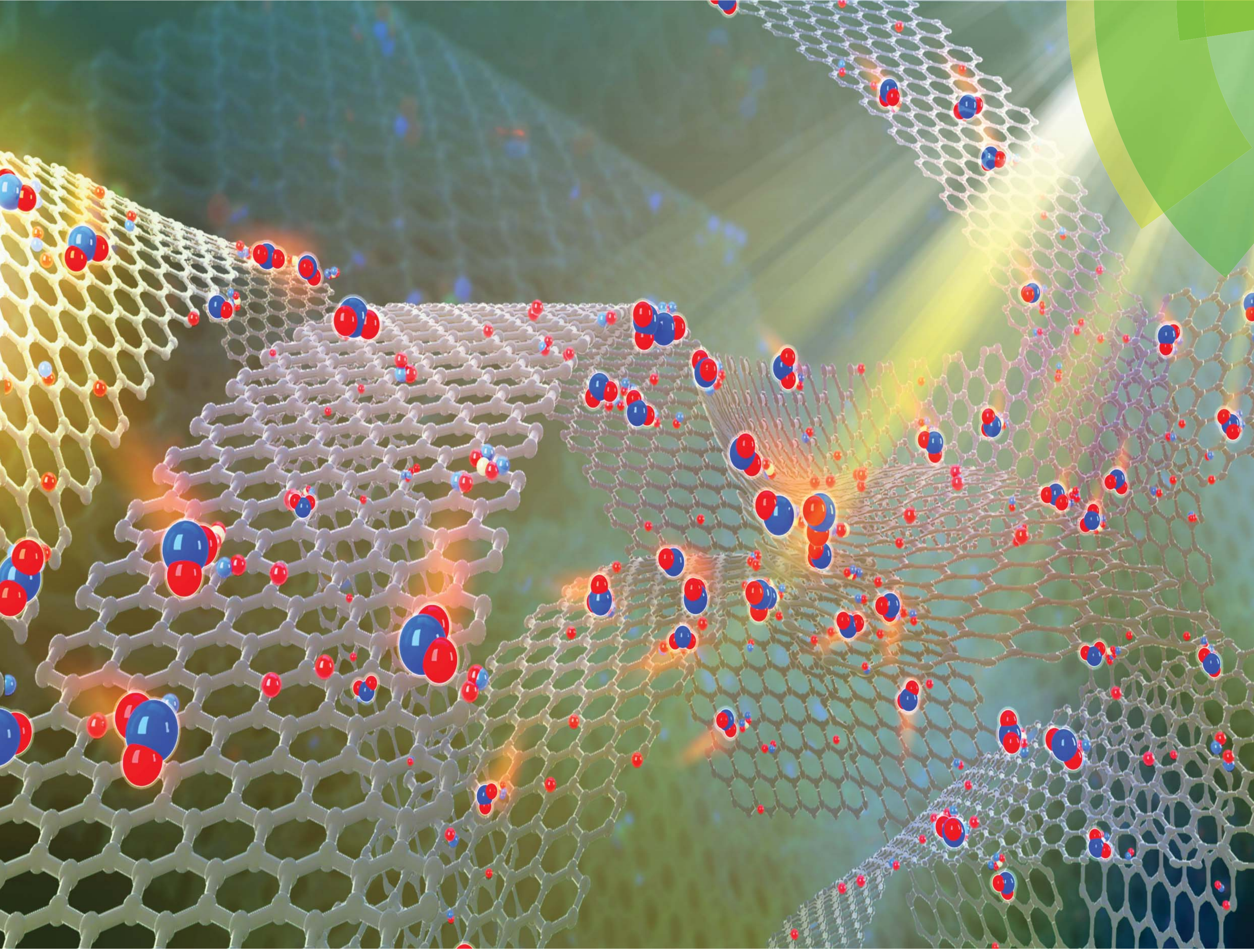

ISSN 2516-0230

ROYAL SOCIETY OF CHEMISTRY | Celebrating IYPT 2019

PAPER
Azhar Ali Haidry, Zhengjun Yao *et al.*
The critical role of hydroxyl groups in water vapor sensing of graphene oxide

NCNST

Nanoscale Advances

PAPER

View Article Online
View Journal | View Issue

Cite this: *Nanoscale Adv.*, 2019, **1**, 1319

The critical role of hydroxyl groups in water vapor sensing of graphene oxide†

Qawareer Fatima,[ab] Azhar Ali Haidry,*[ab] Zhengjun Yao,*[ab] Yue He,[ab] Zhong Li,[ab] Linchao Sun[ab] and Lijuan Xie[ab]

Received 7th August 2018
Accepted 21st October 2018

DOI: 10.1039/c8na00135a

rsc.li/nanoscale-advances

Excellent adsorption of water vapor on the surface of graphene oxide (GO), which contains several inherited functional groups, leads to the development of improved humidity monitoring systems that can urgently meet the high industrial demand. In this study, we fabricated a GO-based humidity sensor and investigated the influence of hydroxyl group concentration on its performance. The sensor exhibited excellent humidity sensing performance in terms of sensitivity (sensor response ~40 for 90% RH), selectivity, stability (both long-term and short-term) and reaction time ($\tau_{res} = 8.5$ s and $\tau_{rec} = 13$ s). Additionally, this sensor does not require external power consumption for heating; thus, the aforementioned performance (recorded at room temperature) with an applied voltage of 0.1 V can significantly reduce the power/energy consumption to about $\sim 1.314 \times 10^{-4}$ kW h per year. In the future, this type of sensor can be integrated into smart humidity monitoring systems to not only monitor but also control the humidity levels on a specific application area. Based on complementary characterization techniques, such as XRD, AFM, Raman and electrical measurement, here, we propose a physical-chemical sensing model to elucidate the aforementioned sensor characteristics.

1. Introduction

In the modern world, the amount of moisture in the air and humidity affects almost all human activities ranging from domestic life to high-tech industries, which can severely impair the usefulness of a process or the characteristics of the resultant product. In this context, a controlled amount of moisture and humidity becomes an indispensable parameter for domestic, industrial and laboratory-based processes.[1] Moreover, due to the existence of moisture everywhere on earth, the demand for moisture and humidity monitoring devices is ever-growing. This demand is not only directly connected with sensitivity, selectivity, stability, accuracy, reproducibility and robustness but also with the ability of the system to control the moisture and humidity level. Thus, we require the development of intelligent humidity monitoring systems that can be utilized not only to detect the exact relative humidity content (%RH) but also to acquaint the feedback system to inject a specific gas to control the %RH at constant level in the process chamber. Such systems are expected to be used in many applications including material processing, food processing and preservation, healthcare, smart homes and industrial fabrication.[1–5] Accordingly, the following text will focus only on graphene oxide-based humidity monitoring sensors. For coherent and logical discussion, the term relative humidity (RH) is used throughout this paper, which corresponds to the ratio of actual atmospheric water vapor concentration to the equilibrium vapor concentration at a given temperature and is expressed in %RH.

Since its discovery, graphene and its derivatives[6,7] have been used in many applications, including oxygen reduction reactions,[8,9] bio-sensing,[10–12] mechanical sensing,[13–15] chemical, and gas sensing.[16] It has been reported that nitrogen doping[8] and Fe–N–C nanoparticles[9] can significantly improve the oxygen reduction reaction (ORR) in energy conversion systems, for instance, in fuel cells and batteries. It has already been demonstrated that resistive-type humidity sensors based on graphene oxide (GO) offer significant solutions to many industries owing to their unique electrical and surface properties[17,18] as well as low-cost fabrication, long-term stability, interchangeability and compatibility with semiconductor fabrication technology.[19] The properties of GO can be enhanced according to the application by controlling its functional groups thermally or *via* chemical reduction since it contains distinct functional groups, *e.g.*, carboxyl, epoxy, lactone, phenol, carbonyl, anhydride, and ether.[20–23] In addition, GO possesses inadmissible defect chemistry and can easily dissolve in water (and organic solvents) due to its oxygen functional groups, which surprisingly give rise to remarkable properties. These functional groups in GO allow fast water permeation within the GO layers,

---

[a] *College of Materials Science and Technology, Nanjing University of Aeronautics and Astronautics, 211100 Nanjing, China. E-mail: aa.haidry@nuaa.edu.cn; azharalig2@gmail.com; yaozj@nuaa.edu.cn*

[b] *Key Laboratory of Materials Preparation and Protection for Harsh Environment, Ministry of Industry and Information Technology, 211100 Nanjing, China*

† Electronic supplementary information (ESI) available. See DOI: 10.1039/c8na00135a

as reported by Nair,[24] which permits rapid water molecule diffusion (in and out of GO) during humidity changes and provides enhanced adsorption and binding energy of gas molecules.[25–27] The respective GO layers are connected *via* H-bonds between the functional groups and water molecules. At high RH, the H-bonds between water molecules dominate, inducing an increase in the distance between the GO layers (so-called swelling effect), which reduces the interlayer H-bond interactions.[28,29] Basically, GO-based gas sensors are p-type materials[30] and show decrease in electrical conduction due to the decrease in surface charge carrier density (in this case, hole concentration) when exposed to humidity. However, despite the rapidly growing interest in utilizing GO-based humidity sensors for real-life applications, almost all the above-mentioned sensors operate at a relatively high applied voltage, which makes them non-compatible for battery operated device applications. Potential solutions to this issue exist, such as using external heating, excessive applied voltage and UV illumination; however, these strategies increase the complexity and cost of the final device.

Various functional groups and defects may act as suitable adsorption sites for particular analyte species on the surface of GO,[31–36] which may become unsuitable for other species. Thus, controlling the concentration of these specific functional groups may lead to the selective detection of a particular chemical species. Although there are several reports on GO-based humidity sensors,[20–33,37–39] there is lack of available literature on the critical role of hydroxyl groups on the humidity sensing properties of GO. To the best of our knowledge, for the first time, herein, the direct impact of hydroxyl groups on the humidity sensing properties of GO is explored. GO samples were fabricated *via* a modified Hummer's method followed by a simple drop casting procedure onto substrates with interdigitated electrodes. The concentration of specific hydroxyl group was controlled by the chemical treatment of GO in ether solution. The prepared sensor showed excellent humidity sensing properties in terms of sensitivity, selectivity, stability and robustness. Importantly, the sensor operates under ambient conditions at 0.1 V and thus it can significantly reduce the overall power consumption, which is highly suitable for battery operated devices.

2. Experimental

2.1 Materials

All chemicals were used as received, unless otherwise mentioned. Commercial GO (0.5 mg mL^{-1} in ethanol) was purchased from Nanjing XFNANO Materials Tech Co. Ltd. For the synthesis of GO in our lab, we used graphite powder (particle size 700 mesh, Squama Carbon 80–99.95%, Qingdao Jinhui Graphite Co. Ltd. China), sulfuric acid (H_2SO_4, 98% pure, Nanjing Chemical Reagents Co., Ltd. China), sodium nitrate ($NaNO_3$, Sinopharm Chemical Reagent Co. Ltd. China), potassium permanganate ($KMnO_4$, 99.5% pure, Sinopharm Chemical Reagent Co. Ltd China), hydrogen peroxide (H_2O_2, 30% pure, Xilong Chemical Co. Ltd. China), and hydrochloric acid (HCL, 37% pure, Nanjing Chemical Reagents Co. Ltd. China). Distilled water (DI-H_2O) was prepared in our lab.

2.2 Graphene oxide synthesis

Graphene oxide was prepared using a modified Hummer's method with different concentrations of oxidizer. The typical GO synthesis procedure is as follows: first, graphite powder (2 g), sulfuric acid (90 mL), and sodium nitrate (2 g) were mixed in a 500 mL flask in an ice bath and continuously stirred for 4 h while maintaining the temperature below 5 °C. Then, 3 g potassium permanganate ($KMnO_4$) was added to the solution gradually to keep the reaction temperature below 14 °C. The reaction mixture was continuously stirred for 2 h at 5 °C. Next, the ice bath was removed, and the mixture was further stirred for 1 h at 35 °C. Then, 90 mL of DI-water was added under rigorous stirring at 90 °C for 1 h. The reaction was then terminated by adding hydrogen peroxide (30%/20 mL) with continuous stirring for 2 h until the solution turned yellow. Subsequently, the obtained solution was filtered and washed with 5% HCl solution and DI-water several times *via* centrifugation. After washing, GO was dried overnight at room temperature under ambient conditions.

Subsequently, GO with different degrees of oxidation was synthesized by changing the content of $KMnO_4$ to 3 g, 6 g, and 12 g. Then, the GO dispersion was dissolved in ethanol for the drop-casting procedure to obtain the GO-based humidity sensors. In the results and discussion sections, commercial GO is labelled as C-GO, and the samples prepared in FuMS are designated as GO. Meanwhile, GO samples prepared with 3 g, 6 g, and 12 g of $KMnO_4$ are labelled as GO-I, GO-II and GO-III, respectively. Based on the initial results and analysis, GO-III was found to be the best contender for humidity sensing. Next, to investigate the effect of hydroxyl groups, GO-III was further functionalized with 2 and 5 mL ether, and these samples were further labelled as E-GO-I and E-GO-II, respectively. For simplicity, GO-flakes are referred to as GO only throughout the text (Table 1).

2.3 Sensor fabrication

For the fabrication of the sensor, we adopted two schemes, as illustrated in Fig. 1. In Scheme 1, the GO-containing solution was drop-casted three times (each drop contained 0.05 mL GO containing solution) onto the ceramic corundum (Al_2O_3) sensor substrates ($L \times W \times T = 10 \times 5 \times 0.65$ mm size) with seven already patterned fingers (or pairs) of gold interdigitated electrodes (IDEs) with a finger length of 0.18 mm and distance of 0.15 mm between consecutive fingers (Changchun Zhaofeng BoRui Technical Co., Ltd). In Scheme 2, the GO containing solution was drop-casted using the same procedure onto polyimide (PI) sensor substrates ($L \times W \times T = 15 \times 5 \times 0.15$ mm

Table 1 The synthetic parameters used to prepare graphene oxide treated with 2 and 5 mL of ether

Sample	GO-III	Ethanol	Ether
GO-III	0.29 g	20 mL	0 mL
E-GO-I	0.29 g	20 mL	2 mL
E-GO-II	0.29 g	20 mL	5 mL

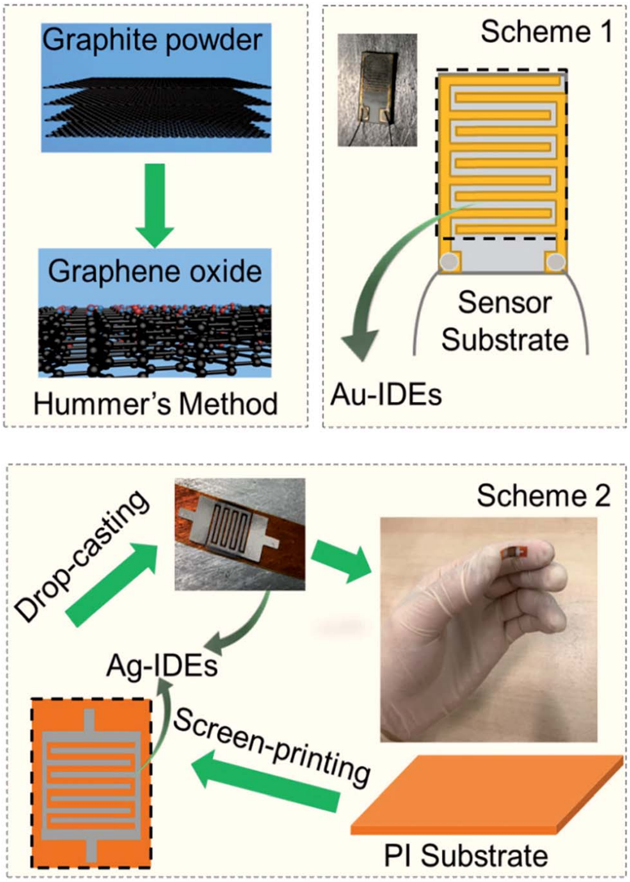

Fig. 1 Schematic showing the Hummer's method and sensor fabrication process, which also shows the drop-casted GO flakes on the ceramic sensor substrate with interdigitated electrodes (IDEs), where the distance between two consecutive Au electrodes is 150 μm (Scheme 1). In Scheme 2, Ag-IDEs (300 μm finger gap) were patterned on polyimide flexible substrates *via* a screen printing method followed by drop-casting of GO. Both schemes also show the respective digital photographs of the final sensor.

size), on which we patterned Ag-IDEs with seven fingers (or pairs) having a finger length of 0.3 mm and distance of 0.3 mm between consecutive fingers. The prepared sensors with schemes were then heated at 150 °C on a hot-plate under ambient conditions for at least 30 minutes to remove any chemical reagent in GO. Thereafter, two different approaches were adopted for the humidity and/or gas sensor tests.

2.4 Humidity tests

Thereafter, two different approaches were adopted for the humidity and/or gas sensor tests. The first approach used a dynamic gas mixing setup, in which high purity gases were used (Jiangsu Tian Hong Chemical Co., LTD) and the sensing measurements were performed in a computer-controlled gas sensing measurement unit at the FuMS laboratory (Functional Materials and Chemical Sensor Lab) College of Materials Science and Technology, Nanjing University of Aeronautics and Astronautics. All the instruments in FuMS were remotely controlled with custom-made LabVIEW software. The sensing setup consisted of five red-y smart mass flow controllers (MFCs) purchased from Vögtlin Instruments (Switzerland) operated under a constant gas flow regime in the range of 10 to 500 standard cubic centimeters (sccm). The constant regime flow was fixed at 400 sccm, and the relative humidity (%RH) was controlled using a gas flow concentration mix of dry technical air (80% N_2 and 20% O_2) as the carrier gas and humid argon (99.99% pure) flowing through a water vapor bubbler. A schematic of this setup is shown in Fig. S1 of the ESI† and further details are available elsewhere.[37,38]

In the second approach, the static RH was obtained at room temperature using various saturated chemical solutions in air-tight glass flasks. For example, NaCl saturated solution was used to produce 75% RH. The schematic together with a table showing the relationship between humidity and used chemicals is shown in Table S1-ESI,† and this approach is shown in Fig. S2-ESI.† In all cases, the actual amount of %RH in the chamber was monitored using a commercial BENETECH Gm1360 Humidity & Temperature Meter purchased from Shenzhen XRC Electronics Co., Ltd.

2.5 Electrical measurements

For electrical measurements, a voltage was applied on the sensor IDEs using a 6482 Dual-Channel Pico ammeter/voltage source (Keithley, Tektronix US) to measure the dynamic changes in the current of the sensor. This device could be used to apply ±30 V DC (direct current) and measure very low currents (up to $\sim 10^{-12}$ A). To ensure good electrical contact between the IDEs of the sensors and low noise tri-axial cable (Model 237-TRX-NG) of the Keithley source meter, very thin Pt wires ($\varnothing = 0.1$ mm) and silver paste solder were used. All humidity measurements were carried out at room temperature. The sensor response (S_R) was estimated using the formula

$$S_R = 100 \times [\Delta I/I_t] = 100 \times [(I_{air} - I_t)/I_t] \quad (1)$$

where I_{air} and I_t (or $I_{\%RH}$) are the stable values of current in air and real time current (or in a defined %RH), respectively. The (i) response (τ_{res}) and (ii) recovery (τ_{rec}) times were estimated for 90% change from (i) I_{air} to $I_{\%RH}$ when exposed to a specific RH and (ii) $I_{\%RH}$ to I_{air} when specific RH exposure was turned (i) ON and (ii) OFF, respectively. The selectivity factor (S_F) was estimated as the response ratio of a specific RH value against other gases.

2.6 Characterization

To investigate the presence of functional groups, the surface topography and height profile of the samples were characterized *via* FTIR, Raman spectroscopy and AFM, respectively. A JASCO 6100 Fourier transform-infrared (FTIR) spectrometer (JASCO International Co., Ltd., Japan) was used to measure the FTIR spectra in the mid-infrared spectral range of 400–4000 cm^{-1} with the IR spectral resolution of 2.00 ± 0.01 cm^{-1}. Raman spectra were measured using a micro-Raman spectrometer Raman (Renishaw inVia Ltd., England) with the excitation laser wavelength $\lambda = 532$ nm and power $P = 5$ mW. Phase composition, crystal structure, and height profile (layer distance) were identified by X-ray diffraction (XRD, Ultima IV, RIGAKU from Japan) with Cu Kα radiation ($\lambda = 0.15406$ nm) in the 2θ range of 10–75° at a scanning rate of 5° min^{-1}. The surface topography and height profile of GO were measured *via* atomic force microscopy (AFM from Suzhou Flyingman Co. Ltd., China) with an Si tip operating in the non-contact mode. In addition, transmission electron microscopy (TEM) images were obtained on a JEM-2100F transmission electron microscope (JEOL Ltd., Japan).

3. Results and discussion

3.1 Sensor performance

First, the humidity sensing was analysed and the performance of the GO-sensors was compared with that of commercial C-GO. Initially, the features of the electrode-GO (Au–GO) interface were investigated *via* current–voltage measurements (*I*–*V*), which were performed from −4 to +4 V under air, argon and humidity backgrounds with a low scan rate of ±0.01 V to ensure reliable analysis, as shown in Fig. 2(a). The obtained *I*–*V* curves confirmed the formation of an ohmic contact at Au–GO interface since they exhibit excellent linear dependency on sensor current at the applied voltage. It is also inferred from the *I*–*V* curves that GO is p-type since the values of the current in air are higher than that in pure argon or humidity ($I_{\mathrm{air}} > I_{\mathrm{Ar}} > I_{\mathrm{RH}}$); for instance, at 1 V, $I_{\mathrm{air}} = 0.736$ mA, $I_{\mathrm{ar}} = 0.714$ mA, and $I_{\mathrm{RH}} = 0.709$ mA. The formation of an ohmic GO-metal electrode interface and decrease in current values under a humid background were observed for all samples, which is in good agreement with the results of previous reports.[39–44] By forming an ohmic contact, the contribution of the GO–Au interface was eliminated and the obtained sensor response is purely given by the only the contribution of the GO-sensing layer in all cases, which makes the humidity sensing analysis uncomplicated. To further confirm the good GO/Au interface, SEM analysis was performed, and the SEM micrographs are shown in Fig. 2(b) and (c). It can clearly be seen from both SEM micrographs that the GO/Au interface is well established to avoid any noise in the sensor signal and any contribution from this interface, as mentioned before.

The argon gas flow cycles 1–9 in Fig. 3(a) correspond to the RH change in the range of 9–90% RH, and these cycles (1–9) and their corresponding RH values (9–90% RH) remain the same throughout the text. As shown in Fig. 3(b), the sensors based on C-GO have better humidity responses at a voltage ≥1 V and the best responses were obtained at an applied voltage of 2 V. For example, the C-GO response values to 44% RH measured at 2, 1 and 0.1 V are 6.31, 4.06, and 2.74, respectively. The response was also significantly reduced at a voltage below 1 V. As clearly seen in Fig. 3(b) (inset), the C-GO response to humidity above 44% RH was highly unstable at 0.1 V, which makes C-GO unsuitable for low voltage battery applications. On the other hand, the sensors based on GO (prepared in FuMS) showed excellent reproducible responses at 0.1 V, as shown in Fig. 3(c) and (d). The response values of GO-I, GO-II and GO-III were much higher than those observed for C-GO. The comparison of the dynamic responses in Fig. 3(c) demonstrates the superior humidity performance of GO-I, GO-II, and GO-III. For example, from the comparative curves in Fig. 3(c), the estimated response values of C-GO, GO-I, GO-II and GO-III to 9% RH are 1.14, 1.57, 2.96, and 3.29, respectively.

Moreover, the GO sensors (prepared in FuMS with 3, 6, and 12 g $\mathrm{KmnO_4}$) showed decent responses to all RH values, as shown in Fig. 3(d). Among them, GO synthesized with 6 and 12 g $\mathrm{KmnO_4}$ showed comparatively improved humidity sensing characteristics. However, the response of the GO-II-based sensor was higher than that of GO-III for low to medium humidity and saturated for humidity higher than 70% RH. Meanwhile, the humidity response increased linearly for the GO-III sensor. These results support the modification of functional groups on the GO samples, and after careful consideration, the GO-III sample was selected as the response does not saturate at high RH. In addition, the correlation factor for GO-II ($R^2 \cong 0.95$) was lower than that of GO-II ($R^2 \cong 0.99$), and Fig. S3-ESI† shows the linear fit comparison of GO-I, GO-II, and GO-III samples. Fig. 4(a) shows the dynamic responses of the GO-III, E-GO-I, and E-GO-II sensors for a broad range of humidity (9–90% RH) measured with 0.1 V at room temperature. The dynamic responses clearly evince the superior humidity characteristics of the sensors treated with ether, *i.e.*, E-GO-I and E-GO-II. The response values of E-GO-I and E-GO-II increased to about 47%

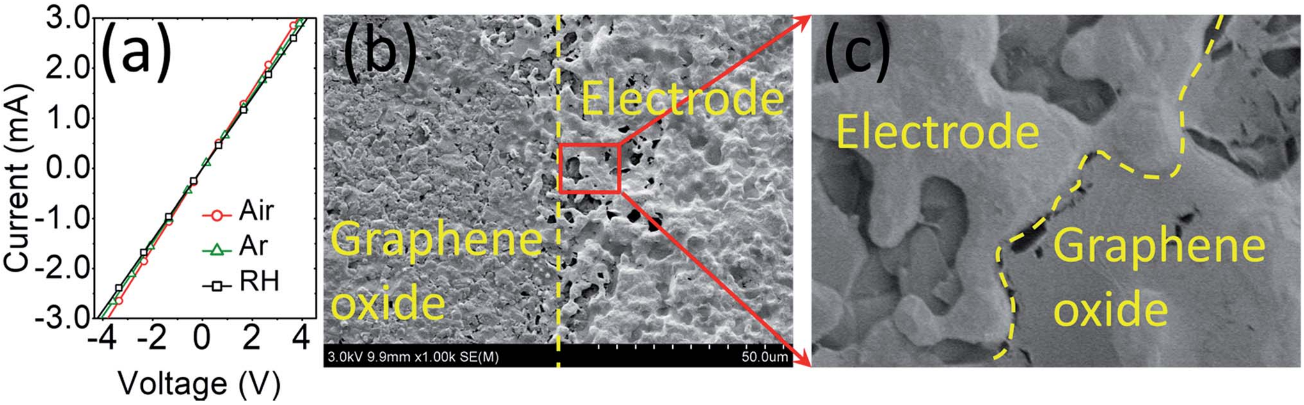

Fig. 2 Current–voltage (*I*–*V*) measurements performed in air, argon and 50% RH with a step size of ±0.01 V (a). SEM micrograph showing the graphene oxide and electrode interface (b), and magnified view of the GO/electrode interface (c).

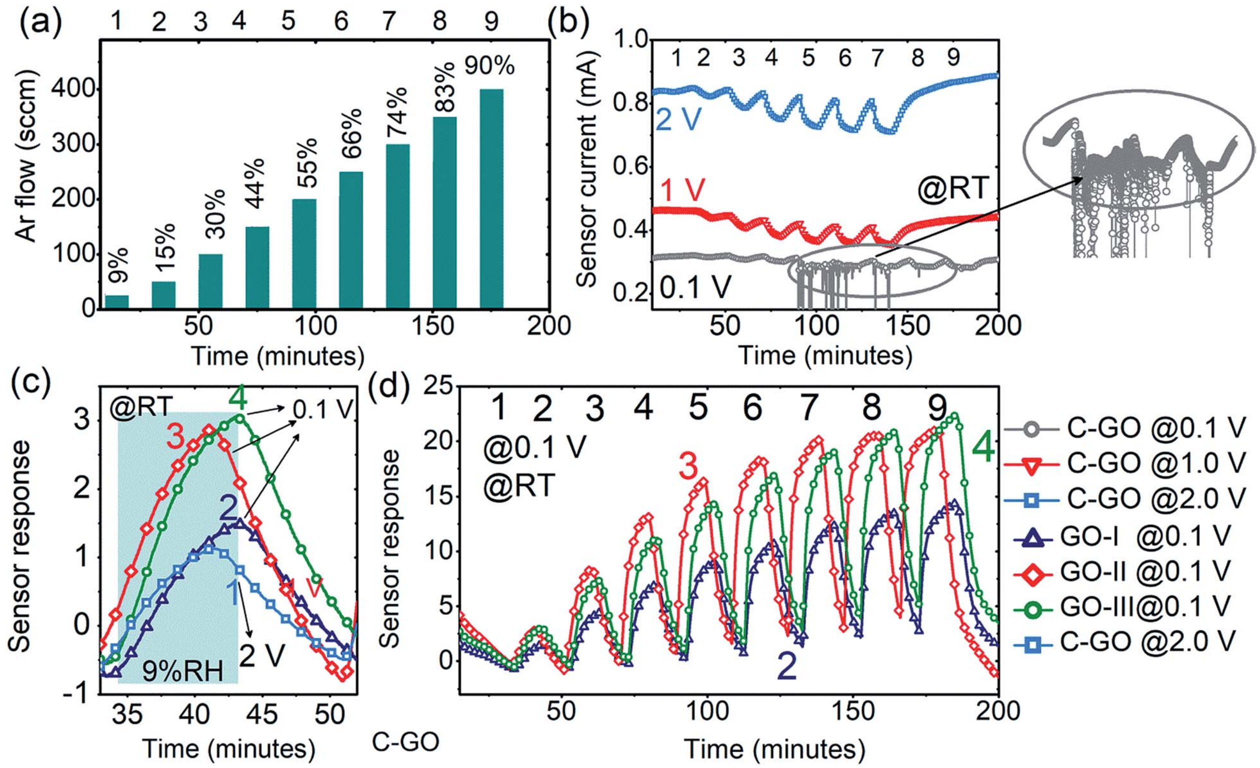

Fig. 3 Argon gas flow (sccm-standard cubic centimetres) cycles 1–9 correspond to a RH change of 9–90% RH, and these cycles and their corresponding RH values remain constant throughout the text (a). Dynamic responses showing real time changes in sensor current with time when exposed to various RH concentrations (9%, 15%, 30%, 44%, 55%, 66%, 74%, 83%, and 90% RH, cycles 1–9 respectively) for commercial GO (C-GO) measured at 2 V (blue color; open square □ symbol), 1 V (red color; open up-triangle △ symbol), and 0.1 V (dark gray color; open circle ○ symbol) (b). Comparative plot of C-GO response to 9% RH measured at the best operating voltage of 2 V (blue color; open square □ symbol), GO-I (navy blue color; open up-triangle △ symbol), GO-II (orange color; open down-triangle ▽ symbol), and GO-III (green color; open circle ○ symbol) measured at 0.1 V (c). Detailed dynamic responses of GO-I, GO-II, and GO-III for a broad range of %RH measured at 0.1 V (d), where all the plot legends are synchronized and shown on the top of (d) and all the measurements were performed at room temperature (@RT).

and 95%, respectively. For example, for 90% RH, the response values of GO-III, E-GO-I, and EGO-II were about 21.3, 30.9 and 38.5, respectively. The plot showing the sensor response comparison of GO-I, GO-II, GO-III, EGO-I, and EGO-II is displayed in Fig. S4-ESI.† In addition, it was observed that the responses of the GO sensors remained unchanged for <0.5 V but destabilized under high %RH when the applied voltage further increased. For instance, at high voltage, as shown in Fig. S5-ESI,† the response of E-GO-I and E-GO-II not only reduced but also became unstable.

Moreover, against other reducing gases, all the sensors at all applied voltages showed no or negligible response to 0.1 vol% of H_2 and CO, as shown in Fig. S6(a)-ESI.† Meanwhile, a slight response to 0.1 vol% CH_4 with 1.0 V at room temperature was obtained, which was not fully recoverable and repeatable with a drift in the baseline current value, as shown in Fig. S6(b)-ESI.† As an example, the estimated selectivity factor, S_F, of E-GO-II for 90% RH measured at 0.1 V against 0.1 vol% H_2, CO, and CH_4 (with 1.0 V) is ∼48, (∼32). This indicates the selectivity of the sensor to RH only. To check the functionality of the sensors with flexible substrates, a solution of E-GO-II was also simultaneously drop-casted onto polyimide (PI) substrates, as shown in Scheme 2 in Fig. 1. The value of the baseline current for the PI/E-GO-II (8.52×10^{-6} A) sample was lower than that of the Al_2O_3/E-GO-II (1.63×10^{-5} A) sample, as shown in Fig. S7-ESI.† Moreover, the response also decreased slightly for Scheme 2, as shown in Fig. 4(b). We believe that the lowering of the baseline current (and sensor response) with PI substrate is strongly related to the electrode material (Ag for PI) and its design, where the distance between the consecutive fingers pair is about 300 μm (>150 μm for Ag IDEs on Al_2O_3 substrate). Next, the sensors were operated outside the sensing chamber under ambient conditions to test their response to human breath, which contains high relative humidity. As evident from Fig. 4(c), the sensor showed a stable response even with PI substrate to continuous exhaling/inhaling cycles. Additionally, a video is provided as a ESI,† which demonstrates the real-time humidity measurement in human breath. The response and recovery time values were unprecedentedly short at about 0.9 and 0.4 seconds, respectively, as shown in Fig. 4(d). This can be correlated to the fact that the measurements were conducted in open air environment, which contains light radiation to enhance the sensor signal.

Further in-depth investigations of the important sensor characteristics (hysteresis, reaction/recovery times and stability) were carried out with the E-GO-II sample prepared on a ceramic substrate, as presented in Fig. 5. The humidity step-like changes (6–30% RH) in Fig. 5(a) with small possible steps (3% RH) in the

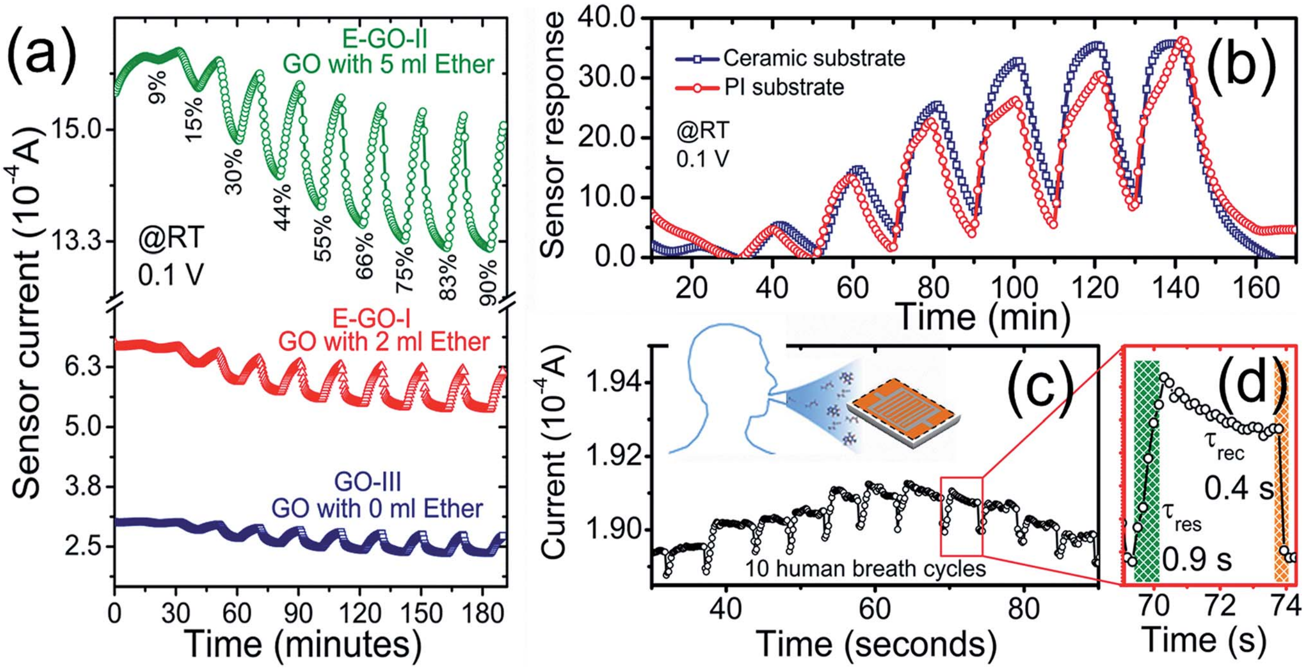

Fig. 4 Comparative dynamic responses of GO-III (0 mL ether), E-GO-I (2 mL ether), and E-GO-II (5 mL ether) measured at 0.1 V room temperature (a) with dynamic responses of GO-III (blue color; open square □ symbol), E-GO-I (red color; open up-triangle △ symbol), and E-GO-II (green color; open circle ○ symbol). Plot of sensor response against time showing a comparison between the E-GO-II sensors prepared on a ceramic substrate (blue color; open square □ symbol) and polyimide substrate (red color; open circle ○ symbol) measured at room temperature with 0.1 V applied voltage (b). One of the typical dynamic response and recovery curves of the E-GO-II sensor prepared on PI substrate with continuous repeated inhaling/exhaling breath monitoring at different rates (c). Inset shows one of the typical single dynamic responses of the same sensor, showing rapid response and recovery with human breath at room temperature under ambient environment (d).

gas flow step correspond to the humidity measurements of E-GO-II and E-GO-I in Fig. 5(b) and (c). The sensor showed recoverable adsorption and desorption reaction even with the small humidity changes, giving an RH accuracy value of ±3–4% RH. The linear fit of the E-GO-I and E-GO-II sensor response against RH value is given in Fig. 5(d), which shows excellent linearity with estimated correlation factor values ($R^2 \cong 0.99$) for both samples. Moreover, the reliability of the sensor performance (so-called short-term stability) was checked with hysteresis curves, which show the difference between the response values of the adsorption and desorption processes at specific %RH. From the hysteresis curves presented in Fig. 5(e), it is clear that both samples do not show striking differences in their adsorption and desorption processes. The only slight difference was observed in the medium humidity range of 40–60% RH, and the maximum difference values in hysteresis were 1.13% and 0.63% towards 44% RH for the E-GO-I and E-GO-II sensors, respectively.

From the dynamic responses, the estimated response (τ_{res}) and recovery (τ_{rec}) times of the sensors are shown in Fig. 5(f), which demonstrate the decrease in both τ_{res} and τ_{rec} with an increase in RH values. For example, the typical τ_{res} (τ_{rec}) value decreased from 7.2 to 1.5 (from 8.1 to 4.3) minutes with RH increasing from 9% to 90% RH. The τ_{res} and τ_{rec} values are even lower for the other samples, as can be seen in Fig. 5(f). On comparison, these τ_{res} and τ_{rec} values are much higher than the values mentioned in previous reports.[39–47] However, we strongly believe that the mentioned τ_{res} and τ_{rec} values in the present case do not represent the actual surface reaction but are rather given by the gas mixing process of the designed sensor test experiment, as already described elsewhere.[48] This was already proven by the breath analysis experiment shown in Fig. 4(d). Thus, to further prove this non-trivial behaviour, we designed a second approach (as mentioned in the Experimental section) to test the sensors under a static measurement system, which was adopted by many researchers in the aforementioned reports. One of the typical E-GO-II dynamic responses measured with the static humidity setup is shown in Fig. S8(a)-ESI,† which clearly demonstrates that the actual τ_{res} and τ_{rec} values are much faster ($\tau_{res} = 8.5$ s and $\tau_{rec} = 13$ s) than that measured with the dynamic gas mixing setup. As realistic evidence, a demonstration of the short reaction times is provided in the supporting Video ESI,† which further confirms our postulate.

Finally, the long-term stability of the sensors was examined as shown in Fig. 5(g). As can be noticed, the sensors showed nearly the same response to almost all RH values throughout a thirteen month period. To further validate this, the response fluctuation value in the sensor response was estimated using $\Delta S_R = 100 \times [S_{Ri} - S_{Rn}]/S_{Ri}$, where, S_{Ri} and S_{Rn} are the initial and nth measurements, respectively. The average fluctuations in the S_R values for all the %RH values were below 1%, which indicates that the fluctuations in long-term stability are ±1 % RH per year. To summarize, the sensor performance in this study is compared with other previous results in Table 2. While

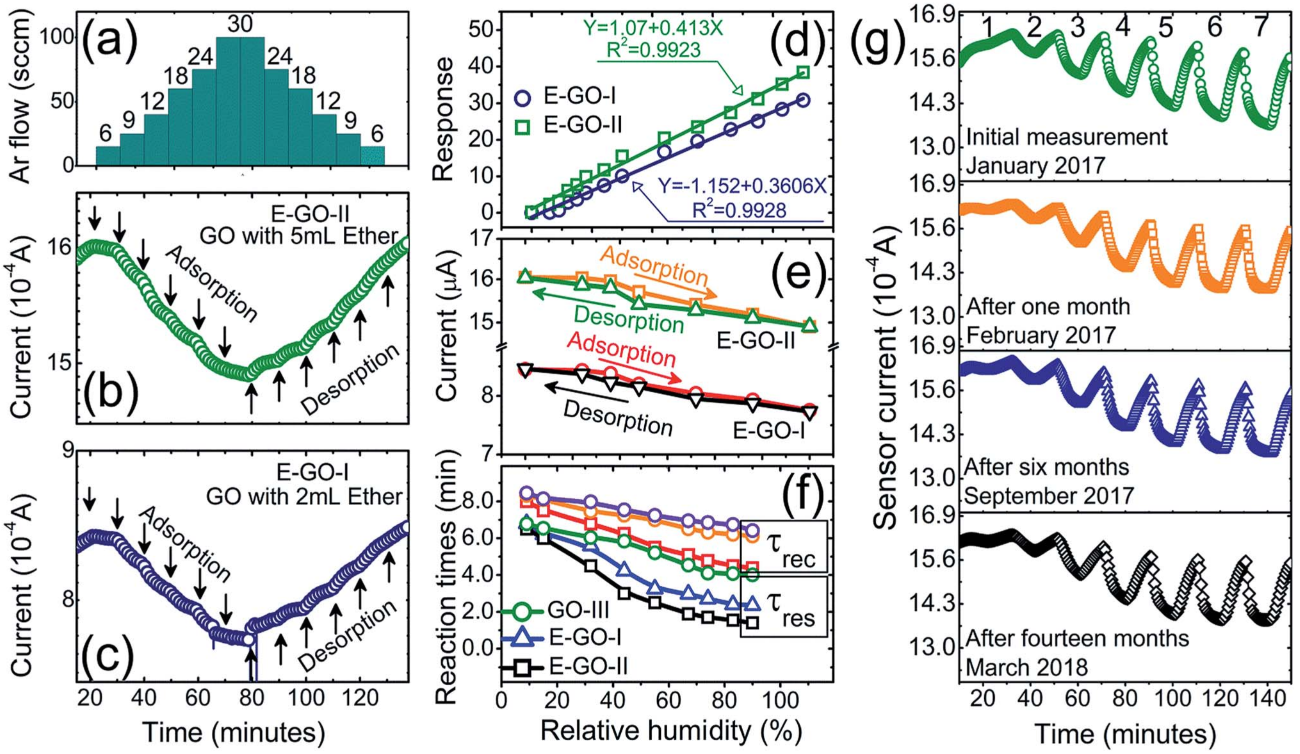

Fig. 5 Step-like RH change from 6–30% RH with small steps (a) and the corresponding step-like changes in the current of the E-GO-I (b) and E-GO-II (c) sensors upon RH adsorption and desorption. Response values (d), adsorption–desorption hysteresis (e) and reaction/recovery times plots (f) of the GO-III, E-GO-I, and E-GO-I sensors under wide range of humidity (6–90% RH). The long-term stability of the sensors was checked and the plot showing one of the repeatable responses of the E-GO-II sensor measured at different times of the year (g).

operating at 0.1 V, the estimated power consumption of the sensor was about 15 μW. Given the above results, the performance of the humidity sensor is definitely suitable for many applications including breath analysis and in the aerospace industry, where the monitoring of trace RH and fog formation near the ground must be remotely recorded as long-term measurements, with an energy consumption $\sim 1.314 \times 10^{-4}$ kW h per year. This value is modest compared with the energy consumed by a normal 60 W bulb, which is ~525.6 kW h per year.

3.2 Discussion

Although there are several reports on GO-based humidity sensors,[31,33,40–44,47,49,50] the water molecule interaction mechanism with the GO surface has always been a controversial discussion in the scientific community. There is a lack of understanding of the GO surface nature and water adsorption, where some authors report GO to behave like an n-type material;[51] on the contrary, some recount it as a p-type material.[42,43] Indeed, there are still numerous unsolved mysteries on the conductivity behaviour of GO and its inversion under humidity; thus, to date, its sensing mechanism remains debatable. Basically, GO is the derived form of organic compounds, having a long chain honeycomb structure of carbon atoms linked with each other either *via* single σ-bond (due to sp^2 hybridization) and/or double/triple π-bond (due to the pz orbital perpendicular to the sp^2 hybrid orbitals). Various inadmissible defects, specifically the functional groups, are the backbone that determine the physical and chemical properties of GO. According to many authors, these single atoms (*e.g.*, oxygen) and molecular (*e.g.*, hydroxyl) functional groups (O, OH^-, C=O, COOH, HOOC; hydroxyl, epoxy, carboxyl, and carbonyl groups) determine the water adsorption/desorption mechanism on the GO surface. Accordingly, we attempted a possible and realistic interpretation of the above sensor performance to elucidate the sensing mechanism based on FTIR, Raman, XRD, and AFM studies.

The main feature of this discussion is the pivotal role of OH^- groups in the enhanced water adsorption/desorption processes. As can be seen from the data obtained from all sensors, the humidity response of GO is directly dependent on the amount of hydroxyl group, as shown in Fig. 6(a). The sensing mechanism showing the complete process of the water adsorption scheme on GO is predicted in Fig. 6(b). Subsequently, the sensing mechanism and its authentication are both discussed simultaneously. In the absence of humidity, *i.e.*, dry air, the electronic conduction is basically dominated by the concentration of surface charge carriers on GO, which in the present case is hole concentration [h^+]. With the initial injection of technical air, a high amount of oxygen enters the sensing chamber, and the current value increases, as shown in Fig. S8(a)-ESI.† A plausible reason for this observation is the dry air surface reaction with functional groups, such as acceptor

Table 2 Comparison of the sensor characteristics in the current study with previously reported characteristics

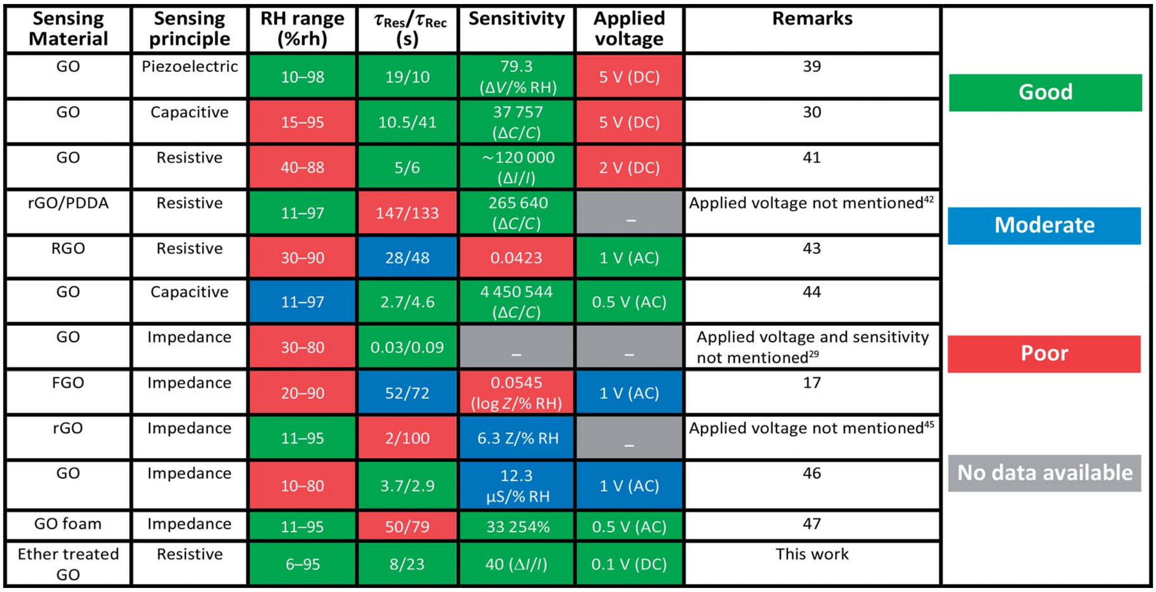

Sensing Material	Sensing principle	RH range (%rh)	τ_{Res}/τ_{Rec} (s)	Sensitivity	Applied voltage	Remarks
GO	Piezoelectric	🟩 10–98	🟩 19/10	🟩 79.3 (ΔV/% RH)	🟥 5 V (DC)	39
GO	Capacitive	🟥 15–95	🟩 10.5/41	🟩 37 757 (ΔC/C)	🟥 5 V (DC)	30
GO	Resistive	🟥 40–88	🟩 5/6	🟩 ~120 000 (ΔI/I)	🟥 2 V (DC)	41
rGO/PDDA	Resistive	🟩 11–97	🟥 147/133	🟩 265 640 (ΔC/C)	⬜ –	Applied voltage not mentioned[42]
RGO	Resistive	🟥 30–90	🟦 28/48	🟥 0.0423	🟩 1 V (AC)	43
GO	Capacitive	🟦 11–97	🟩 2.7/4.6	🟩 4 450 544 (ΔC/C)	🟩 0.5 V (AC)	44
GO	Impedance	🟥 30–80	🟩 0.03/0.09	⬜ –	⬜ –	Applied voltage and sensitivity not mentioned[29]
FGO	Impedance	🟥 20–90	🟦 52/72	🟥 0.0545 (log Z/% RH)	🟦 1 V (AC)	17
rGO	Impedance	🟩 11–95	🟥 2/100	🟦 6.3 Z/% RH	⬜ –	Applied voltage not mentioned[45]
GO	Impedance	🟥 10–80	🟩 3.7/2.9	🟦 12.3 μS/% RH	🟦 1 V (AC)	46
GO foam	Impedance	🟩 11–95	🟥 50/79	🟩 33 254%	🟩 0.5 V (AC)	47
Ether treated GO	Resistive	🟩 6–95	🟩 8/23	🟩 40 (ΔI/I)	🟩 0.1 V (DC)	This work

🟩 Good
🟦 Moderate
🟥 Poor
⬜ No data available

OH^-, which creates more holes and hence increases its concentration $[h^+]$. Similarly, the current increases due to the change in chamber environment from a humid to an oxygen-rich environment. In addition, as can be seen from Fig. 3 and 4, the current values decrease with an increase in $KMnO_4$ (I_{air} [A] $= 0.8 \times 10^{-3}$, 1.25×10^{-4}, and 3.28×10^{-4} for GO, GO-II, and GO-III, respectively) and ether contents (I_{air} [A] $= 8.17 \times 10^{-4}$ and 16.15×10^{-4} for E-GO-I and E-GO-II, respectively). The reason for this phenomenon is discussed further.

It is conclusively evident from the estimated transmittance ($\Delta T = T_{initial} - T_{final}$) values presented in the 3D bar graphs in Fig. 7(a) for various functional groups and the complete FTIR spectra of the samples in Fig. S9-ESI† that the transmittance intensity of the broad infrared band peak in the range of $\nu = 3600$–2400 cm^{-1} significantly increases with $KMnO_4$ ($\Delta T_{\nu O\text{–}H} = 9$, 22, 24 and 32 for C-GO, GO-I, GO-II and GO-III samples, respectively) and ether contents ($\Delta T_{\nu O\text{–}H} = 35$ and 42 for E-GO-I and E-GO-II samples, respectively). This peak is basically assigned to the stretching modes of the O–H bonds originating from the intercalated water between the graphene oxide layers and the OH^- groups from tertiary alcohol. Here, it is reasonable to infer that the increase in peak intensity is due to the OH^- functional

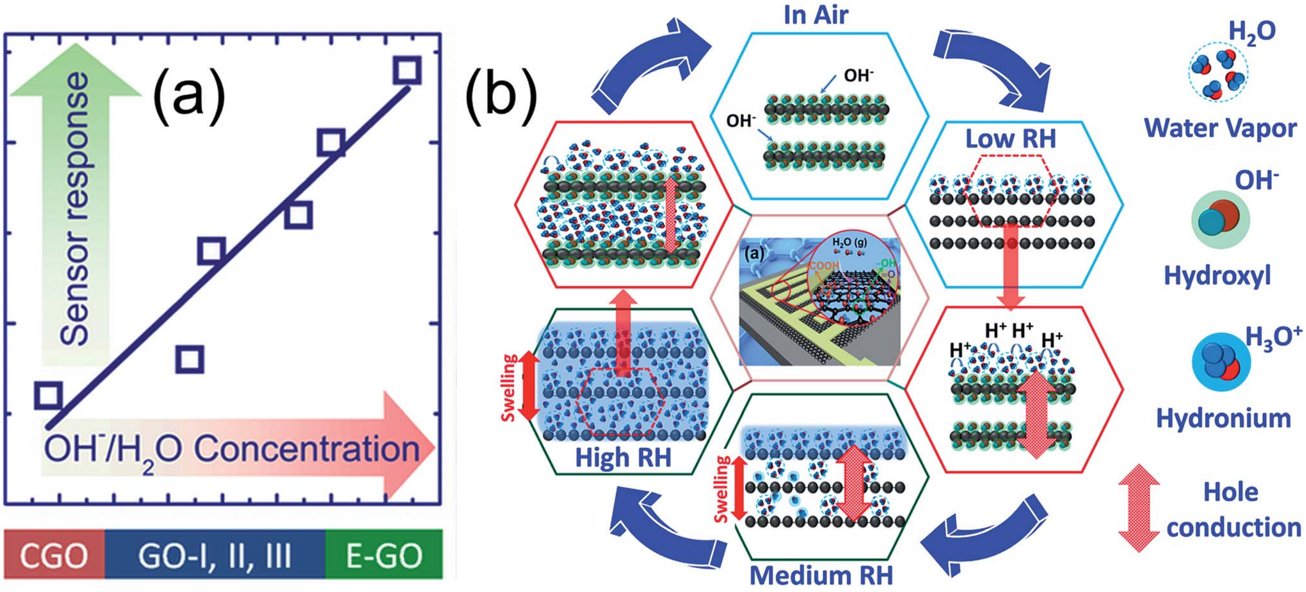

Fig. 6 Interdependence of humidity response and amount of hydroxyl groups (a). The sensing mechanism proposed based on the results obtained from FTIR, XRD, AFM and Raman spectroscopy. The reaction of water vapor with various functional groups in low, medium and high humidity; the schematic also shows the swelling effect and water, hydroxyl, hydronium, and hole conducting channels on the right (b).

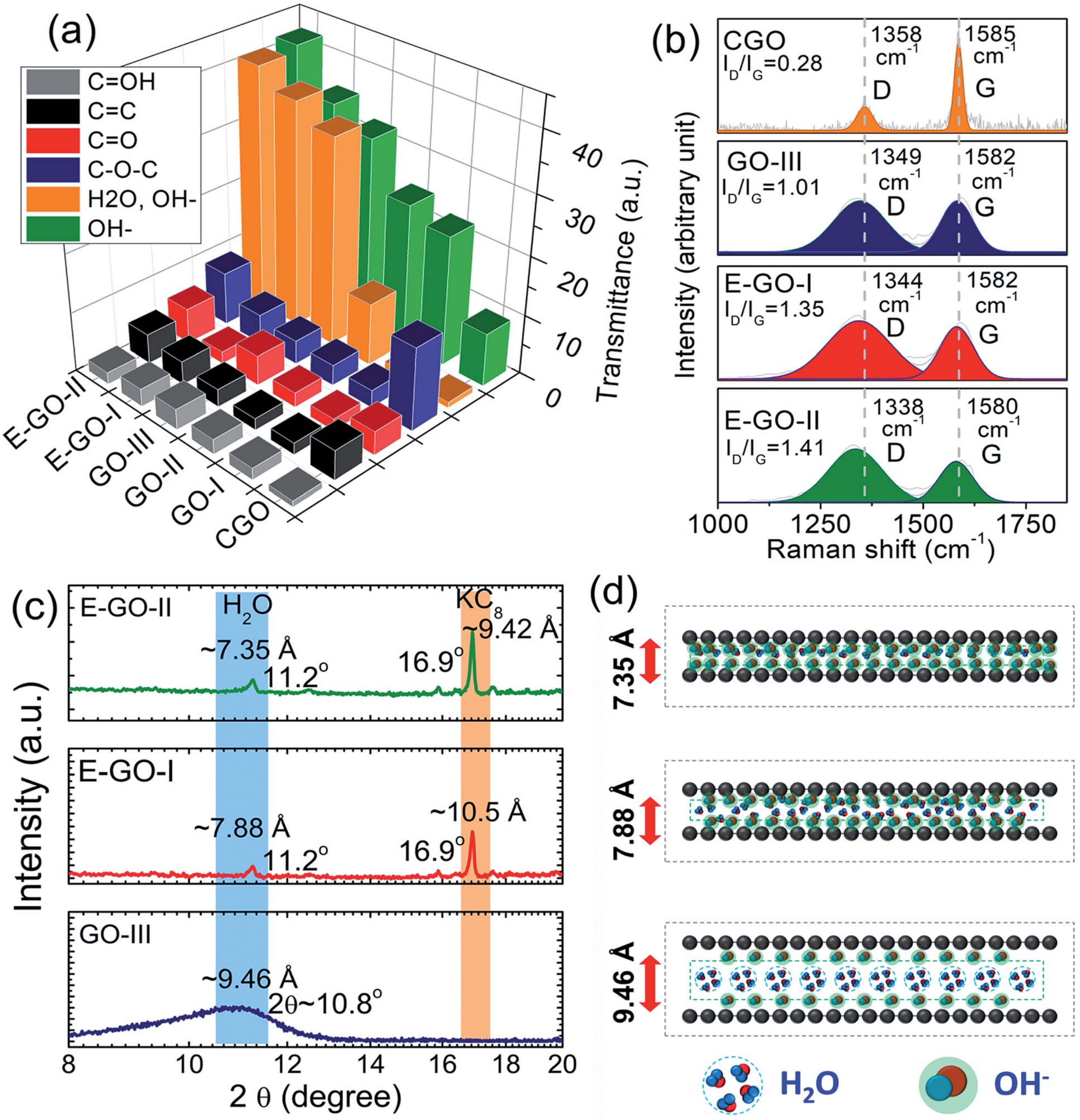

Fig. 7 3D plot of the FTIR analysis of the C-GO, GO-III, E-GO-I and E-GO-II samples showing the variation in various functional group intensities; among them, the hydroxyl and hydrogen-bonded functional group intensities increased significantly with ether treatment (a). Raman spectra of the C-GO, GO-III, E-GO-I and E-GO-II samples (b), which contain two critical D-band and G-band variations with ether treatment, and the I_D/I_G values are also included. XRD diffractograms and the respective illustrated height profiles of the GO-III, E-GO-I and E-GO-II samples are shown in (c) and (d), respectively.

groups rather than intercalated water. This can be proven by two strong reasons: (1) as reported,[52] ether is a strong agent to remove (or condense in solid form) intercalated water and hence (2) to decrease interatomic distance, which will be discussed later in detail. In addition, the bands of the carbonyl moieties and carboxyl groups present in the FTIR spectra at 1650, 1550, 1404, 1100, 1120, and 580 (cm^{-1}) correspond to C═O ($\nu_{C=O}$), C═C ($\nu_{C=C}$), C–OH (ν_{C-O-H}), C–O–C (ν_{C-O-C}), and C═OH ($\nu_{O=H}$), which exist along the GO sheet edges and basal planes.[50,52] The peak intensity of C–OH (ν_{C-O-H}) shows a similar increasing trend (for $KMnO_4$ and ether treatment) to the C–OH (ν_{C-O-H}) band, as shown in Fig. 7(a). Besides, the C–O–C (ν_{C-O-C}) band for C-GO is the maximum, showing the strong correlation of carbon atoms attached to functionalized oxygen.

Due to its sensitive nature to the GO electronic structure, Raman spectroscopy was employed to gain more scientific insights into the crystal disorder and chemical modification due to functional groups. The Raman spectra of C-GO, GO-III, E-

GO-I and E-GO-II are shown in Fig. 7(b). All the samples show D (at $\sim$1358 cm^{-1}) and G (at $\sim$1585 cm^{-1}) bands, which are ascribed to defect-activated sp^3-bonded doubly resonant disorder defects and sp^2-bonded in-plane vibration (E_{2g} phonons having in frequency mode at Γ-point) of carbon atoms, respectively. The D-band intensity of C-GO is very low, whereas the G-band intensity is very high for GO-III, E-GO-I, and E-GO-II; in the latter case, the band also broadens and shifts to the left, as can be observed in Fig. 7(b). This small left-shift (so-called blue-shift) was also observed for the GO flakes treated with ether (*i.e.*, E-GO-I and E-GO-II), indicating a decrease in the GO-stacked layer thickness. As shown in the Fig. 7(b), the intensity ratio ($R = I_D/I_G$) of the D and G bands, which also represents the structural regularity in GO flakes, still remained in the "low" defect density regime and increased with ether treatment. For instance, the *R*-values for the C-GO, GO-III, E-GO-I, and E-GO-II samples were 0.28, 1.01, 1.35, and 1.41, respectively. These observations indicate an increase in the number of defects due an increase in functional groups, thus causing a more disordered GO structure and shrinking of the layer distance due to ether treatment, which confines the intercalated water from translating into a solid structure.[52]

The shrinking of the layer distance is clearly seen in the measured AFM height profiles of the ether-treated samples in Fig. S10-ESI.† Despite the good agreement with previous results,[36,41,43,44,49,50] we believe that the AFM technique is not very conclusive and only provides a rough estimate about the height profile of the GO layers because controlling the quantity of GO flakes in a drop for AFM analysis is nearly improbable. Moreover, the estimated height profile comes from the GO-stacked layers (aggregated flakes) rather than two consecutive layers.

Narrowing of the GO layers is also observable from the XRD diffractograms presented in Fig. 7(c). Both the E-GO-I and E-GO-II samples show a sharp peak in the 001 direction (perpendicular to the GO plane) at $2\theta = 11.24°$, which corresponds to the GO lattice structure orientation; meanwhile, for GO-III, a broad peak appears at 10.8°. The *d*-value estimated with the procedure mentioned in[51,52] for the GO-III sample ($\sim$9.46 Å) is much higher than that for E-GO-I (7.88 Å) and E-GO-II (7.35 Å). The *d*-value of the as-prepared sample is higher due to the presence of functional groups and abundant intercalated water, as illustrated in Fig. 7(d). The *d*-value of the ether-treated sample decreased to 7.35 Å and the peak sharpened and shifted to right at 11.24°, which is most probably due to the simultaneous increase in functional groups at the graphene basal plane and removal of intercalated water between the layers. The emergence of potassium–carbon (KC_8) is also noticeable for the ether-treated GO, which is because $KMnO_4$ reacted with graphite during the synthesis.[52]

As can be seen from Fig. 3 and 4, GO shows p-type sensing behaviour, which is most probably due to the introduced defects during the Hummer's method, on which adsorbed water vapor is polarized. For GO, the improved sensing characteristics is attributed to the strong adsorption of water molecules on GO-flakes. In this particular case, H_2O is an excellent electron donor, which can enrich the electron concentration in GO to decrease hole density, leading to a decrease in current. At low humidity (in the present case 6–20% RH), water vapor gets adsorbed on the GO surface and spontaneously reacts with the GO surface and functional groups, which are most probably hydrophilic. As a result, water molecules form a network on the GO surface *via* hydrogen bonding and transfer of protons between the adsorbed water and hydrophilic groups (termed proton hopping mechanism) occurs. At this stage, physisorption of the weak mono-layer of water derivatives is possible due to low humidity ($H_2O \leftrightarrow H^+ + OH^-$). Subsequently, as the reaction of the hole charge carrier [h$^+$] at the GO surface is reduced, the current also decreases. In general, at low RH, the concentration of hydronium ions (H_3O^-) is very low due to high ionization activation energy, which may be the possible reason that some sensors (including C-GO) do not exhibit a response to low RH. Meanwhile, for the ether-treated samples, numerous defects decreased the ionization energy to yield decent responses even at very low RH (for instance, 6%, 9%, 12% and 18% RH), as shown in Fig. 5(b) and (c).

At medium humidity (in the present case, 20–65% RH), water molecules can form a continuous physisorbed layer on the GO surface and can also possibly permeate within the GO layerso. Thus, both processes determine the sensor response, which is due to H_2O infiltration in the GO layer expanding its thickness (swelling effect). In addition to the physisorption process, Grotthus chain reactions occur to strongly dissociate H_2O into hydronium and hydroxyl ions ($2H_2O \leftrightarrow H_3O^+ + OH^-$), which thus contributes significantly to the humidity sensing mechanism. With a further increase in RH (high humidity 65–95% RH), multilayers of physisorbed water forming a liquid phase on the surface as well as between the GO layers are highly probable, yielding a high amount of H_3O^+ ions. Thus, the current further decreases to decrease the charge carrier concentration.

Based on the above interpretation, it is inferred that the superior humidity sensing of E-GO samples can be correlated with the increased number of hydroxyl groups (FTIR analysis), which play a decisive role to provide a great number of adsorption sites. Specifically, surface reaction mechanism enhancement is strongly expected, unless it is limited by other chemical species, as in the case of the C-GO sensor. In addition, the permeation of water molecules within the GO layers in E-GO is very strong, giving rise to significant GO flake swelling. More importantly, both the adsorption and desorption processes at low and medium humidity are very efficient to give almost full recovery. Specifically, the former process dominates at high humidity, as can be seen in Fig. 4 and 5, where recovery results in a small shift in the sensor signal. Despite this comprehensive analysis and discussion, we believe that the effect of annealing temperature on GO electrical transport and sensor response still needs to be investigated, and the typical comparative responses of the un-annealed and annealed samples are shown in Fig. S11-ESI.† Research activities on these issues are underway in our laboratory.

4. Conclusion

We demonstrated the fabrication of humidity sensors based on GO, which can detect a wide range of humidity (6–95% RH) with an applied voltage of 0.1 V. The static test response time (8 s) and recovery time (13 s) are rapid with excellent stability, RH accuracy value of ±3–4% RH and power consumption of 1.314×10^{-4} kW h per year. The sensors do not show striking differences in adsorption and desorption processes, and the maximum hysteresis value (0.63%) is observed in only the narrow RH middle range (40–60%). The breakthrough data on the functional groups are obtained from FTIR, XRD and Raman analysis, which suggest that hydroxyl groups are the major contributing species, resulting in an enhanced humidity performance. Based on the quality analysis, we proposed a sensing model that fitted exceptionally well with the obtained results. Thus, we believe that the presented results and discussed analysis provide significant conceptual and technological advances for the development of novel gas sensor technology for enhanced and selective monitoring of specific gas species.

Conflicts of interest

There are no conflicts to declare.

Acknowledgements

This project is financially supported by the Priority Academic Program Development of Jiangsu Higher Education Institutions (PAPD), Natural Science Foundation of Jiangsu Province project (BK20170795), National Natural Science Foundation of China (51850410506) and Opening Project (56XCA17006-3) from Key Laboratory of Materials Preparation and Protection for Harsh Environment (Nanjing University of Aeronautics and Astronautics), Ministry of Industry and Information Technology. Dr Azhar Ali Haidry also thanks NUAA for providing start-up funding project.

Notes and references

1 H. Farahani, R. Wagiran and M. N. Hamidon, Humidity sensors principle, mechanism, and fabrication technologies, *Sensors*, 2014, **14**, 7881–7939.

2 Z. Chen and C. Lu, Humidity sensors: A Review of materials and mechanisms, *Sens. Lett.*, 2005, **3**, 274–295.

3 N. Yamazoe and Y. Shimizu, Humidity sensors: Principles and applications, *Sens. Actuators*, 1986, **10**, 379–398.

4 C.-Y. Lee and G.-B. Lee, Humidity sensors: A review, *Sens. Lett.*, 2005, **3**, 1–15.

5 B. H. Lee, W. H. Khoh, A. K. Sarker, C. H. Lee and J. D. Hong, A High performance moisture sensor based on ultra large graphene oxide, *Nanoscale*, 2015, **7**, 17850–17811.

6 C. Wang, M. Zhao, J. Li, J. Yu, S. Sun, S. Ge, X. Guo, F. Xie, B. Jiang, E. K. Wujcik, Y. Huang, N. Wang and Z. Guo, Silver nanoparticles/graphene oxide decorated carbon fiber synergistic reinforcement in epoxy-based composites, *Polymer*, 2017, **131**, 263e271.

7 Z. Yang, X. Hao, S. Chen, Z. Ma, W. Wang, C. Wang, L. Yue, H. Sun, S. Qian, V. Murugadoss and Z. Guo, Long-term antibacterial stable reduced graphene oxide nanocomposites loaded with cuprous oxide nanoparticles, *J. Colloid Interface Sci.*, 2019, **533**, 13–23.

8 Y. Zhang, K. Fugane, T. Mori, L. Niu and J. Ye, Wet chemical synthesis of nitrogen-doped graphene towards oxygen reduction electrocatalysts without high-temperature pyrolysis, *J. Mater. Chem.*, 2012, **22**, 6575.

9 Y. Zhang, L. Qian, W. Zhao, X. Li, X. Huang, X. Mai, Z. Wang, S. Qian, X. Yan and Z. Guo, Highly Efficient Fe–N–C Nanoparticles Modified Porous Graphene Composites for Oxygen Reduction Reaction, *J. Electrochem. Soc.*, 2018, **165**(9), H510–H516.

10 Y. Lu, M. C. Biswas, Z. Guo, J.-W. Jeonb and E. K. Wujcik, Recent developments in bio-monitoring *via* advanced polymer nanocomposite-based wearable strain sensors, *Biosens. Bioelectron.*, 2019, **123**, 167–177.

11 Y. Li, B. Zhou, G. Zheng, X. Liu, T. Li, C. Yan, C. Cheng, K. Dai, C. Liu, C. Shen and Z. Guo, Continuously prepared highly conductive and stretchable SWNT/MWNT synergistically composited electrospun thermoplastic polyurethane yarns for wearable sensing, *J. Mater. Chem. C*, 2018, **6**, 2258.

12 Y. Li, T. Jing, G. Xu, J. Tian, M. Dong, S. Qian, B. Wang, Z. Wang, Y. Zheng, C. Yang and Z. Guo, 3-D magnetic graphene oxide-magnetite poly(vinyl alcohol) nanocomposite substrates for immobilizing enzyme, *Polymer*, 2018, **149**, 13e22.

13 L. Hu, Y. Li, K. Dai, G. Zheng, C. Liu, C. Shen, X. Yan, J. Guo and Z. Guo, Electrically conductive thermoplastic elastomer nanocomposites at ultralow graphene loading levels for strain sensor applications, *J. Mater. Chem. C*, 2016, **4**, 157.

14 L. Hu, M. Dong, W. Huang, J. Gao, K. Dai, J. Guo, G. Zheng, C. Liu, C. Shena and Z. Guo, Lightweight conductive graphene/thermoplastic polyurethane foams with ultrahigh compressibility for piezoresistive sensing, *J. Mater. Chem. C*, 2017, **5**, 73.

15 C. Hu, Z. Li, Y. Wang, J. Gao, K. Dai, G. Zheng, C. Liu, C. Shen, H. Song and Z. Guo, Comparative assessment of the strain-sensing behaviors of polylactic acid nanocomposites: reduced graphene oxide or carbon nanotubes, *J. Mater. Chem. C*, 2017, **5**, 2318.

16 L. Hu, W. Huang, X. Yang, K. Dai, G. Zheng, C. Liu, C. Shen, X. Yan, G. Jiang and Z. Guo, Organic vapor sensing behaviors of conductive thermoplastic polyurethane-graphene nanocomposites, *J. Mater. Chem. C*, 2016, **4**, 4459.

17 P. Guey su and Z. Mao Lu, Flexibility and electrical and humidity sensing properties of diamine-functionalized graphene oxide films, *Sens. Actuators, B*, 2015, **211**, 157–163.

18 P. Suvarnaphaet and S. Pechprasarn, Graphene-Based Materials for Biosensors: A Review, *Sensors*, 2017, **17**, 2161.

19 J. Fontes, *Humidity sensor in sensor technology Handbook*, ed. John S. Wilson, Elsevier Inc., USA, 2005.

20 J. G. Contreras and F. C. Briones, Graphene Oxide powders with different oxidation degree, prepared by synthesis variations of the Hummers method, *Mater. Chem. Phys.*, 2015, **153**, 209–220.

21 L. B. Casabianca, M. A. Shaibat, W. W. Cai, S. Park, R. Piner, R. S. Ruoff, *et al.*, NMR-based structural modeling of graphite oxide using multidimensional 13C solid-state

NMR and *ab initio* chemical shift calculations, *J. Am. Chem. Soc.*, 2010, **132**, 5672–5676.

22 J. L. Figueiredo, M. F. R. Pereira, M. M. A. Freitas and J. J. M. Orfao, Modification of the surface chemistry of activated carbons, *Carbon*, 1999, **37**, 1379–1389.

23 A. Allahbakhsh, A. H. Haghighi and M. Sheydaei, Poly(ethylene trisulfide)/graphene oxide nanocomposites, *J. Therm. Anal. Calorim.*, 2017, **128**, 427–442.

24 R. R. Nair, H. A. Wu, P. N. Jayaram, I. V. Grigorieva and A. K. Geim, Unimpeded Permeation of Water through Helium–Leak–Tight Graphene-Based Membranes, *Science*, 2012, **335**, 442–444.

25 W. H. Lim, Y. K. Yap, W. Y. Chong and H. Ahmad, All Optical Graphene Oxide Humidity sensors, *Sensors*, 2014, **14**, 24328–24337.

26 V. Singh, D. Joung, L. Zhai, S. Das, S. I. Khondaker and S. Seal, Graphene based materials: Past, Present, Future, *Prog. Mater. Sci.*, 2011, **56**, 1178–1271.

27 Y. R. Choi, *et al.*, Role of oxygen functional groups in graphene oxide for reversible room temperature NO_2 sensing, *Carbon*, 2015, **91**, 178–187.

28 N. V. Medhekar, A. Ramasubramaniam, R. S. Ruoff and V. B. Shenoy, Hydrogen Bond Networks in Graphene Oxide Composite Paper: Structure and Mechanical Properties, *ACS Nano*, 2010, **4**, 2300–2306.

29 S. Borini, R. White, D. Wei, M. Astley, S. Haque, E. Spigone, N. Harris, J. Kivioja and T. Ryhanen, Ultrafast Graphene Oxide Humidity Sensors, *ACS Nano*, 2013, **7**, 11166–11173.

30 D. T. Phan and G. S. Chung, P–N Junction Characteristics of Graphene Oxide and reduced graphene oxide on n-type Si(111), *J. Phys. Chem. Solids*, 2013, **74**, 1509–1514.

31 C. Bariain, I. R. Matias, F. J. Arregui and M. Lopez-Amo, Optical Fiber Humidity Sensor based on a tapered fiber coated with agarose gel, *Sens. Actuators, B*, 2000, **69**, 127–131.

32 C. Bian, M. Hu, R. Wang, T. Gang, R. Tong, L. Zhang, T. Guo, X. liu and X. Qiao, Optical Fiber Humidity sensor based on the direct response of the Polyimide film, *Appl. Opt.*, 2018, **57**, 356–361.

33 D. T. Phan and G. S. Chung, Effects of rapid thermal annealing on humidity sensor based on Graphene Oxide thin films, *Sens. Actuators, B*, 2015, **220**, 1050–1055.

34 N. Justh, B. Berke, K. Laszlo and I. M. Szilagyi, Thermal analysis of the improved Hummers' synthesis of graphene oxide, *J. Therm. Anal. Calorim.*, 2018, **131**, 2267–2272.

35 W. S. Hummers and R. E. Offeman, Preparation of graphitic oxide, *J. Am. Chem. Soc.*, 1958, **80**, 1339–1343.

36 N. I. Kovtyukhova, P. J. Ollivier, B. R. Martin, *et al.*, Layer-by-layer assembly of ultrathin Composite films from micron-sized graphite oxide sheets and polycations, *Chem. Mater.*, 1999, **11**, 771–778.

37 L. Sun, *et al.*, Improving the humidity sensing below 30% RH of TiO_2 with GO modification, *Mater. Res. Bull.*, 2018, **99**, 124–131.

38 Z. Li, A. A. Haidry, B. Gao, T. Wang and Z. Yao, The effect of Co-doping on the humidity sensing properties of ordered mesoporous TiO, *Appl. Surf. Sci.*, 2017, **412**, 638–647.

39 Y. Yao, X. D. Chen, H. H. Guo, Z. Q. Wu and X. Y. Li, Humidity sensing behaviors of graphene oxide-silicon bi-layer flexible structure, *Sens. Actuators, B*, 2012, **161**, 1053–1058.

40 H. Bi, K. Yin, X. Xie, J. Ji, S. Wan, L. Sun, M. Terrones and M. S. Dresselhaus, Ultrahigh humidity sensitivity of graphene oxide, *Sci. Rep.*, 2013, **3**, 2714.

41 S. Ghosh, R. Ghosh, P. K. Guha and T. K. Bhattacharyya, Humidity Sensor Based on High Proton Conductivity of Graphene Oxide, *IEEE Trans. Nanotechnol.*, 2015, **14**, 931–937.

42 D. Z. Zhang, J. Tong and B. K. Xia, Humidity-sensing properties of chemically reduced graphene oxide/polymer nanocomposite film sensor based on layer-by-layer nano self-assembly, *Sens. Actuators, B*, 2014, **197**, 66–72.

43 P.-G. Su and C.-F. Chiou, Electrical and humidity-sensing properties of reduced graphene oxide thin film fabricated by layer-by-layer with covalent anchoring on flexible substrate, *Sens. Actuators, B*, 2014, **200**, 9–18.

44 P. He, J. R. Brent, H. Ding, J. Yang, D. J. Lewis, P. O'Brien and B. Derby, Fully printed high performance humidity sensors based on two-dimensional materials, *Nanoscale*, 2018, **10**, 5599.

45 L. Guo, H. B. Jiang, R. Q. Shao, Y. L. Zhang, S. Y. Xie, J. N. Wanf, X. B. Li, F. Jiang, Q. D. Chen, T. Zhang and H. B. Sun, Two-beam-laser interference mediated reduction, patterning and nanostructuring of graphene oxide for the production of a flexible humidity sensing device, *Carbon*, 2012, **50**, 1667–1673.

46 E. U. Park, B. I. Choi, J. C. Kim, S. B. Woo, Y. G. Kim, Y. Choi and S. W. Lee, Correlation between the sensitivity and the hysteresis of humidity sensors based on graphene oxides, *Sens. Actuators, B*, 2018, **258**, 255–262.

47 X. Feng, W. Chen and L. Yan, Free-standing dried foam films of graphene oxide for humidity sensing, *Sens. Actuators, B*, 2015, **215**, 316–322.

48 A. Ali Haidry, L. Sun, B. Saruhan, A. Plecenik, P. Tomas, H. Shen and Z. Yao, Cost-effective fabrication of polycrystalline TiO_2 with tunable n/p conductivity for selective hydrogen monitoring, *Sens. Actuators, B*, 2018, **274**, 10–21.

49 V. H. Pham, T. V. Cuong, S. H. Hur, *et al.*, Chemical functionalization of graphene sheets by solvothermal reduction of a graphene oxide suspension in *N*-methyl-2-pyrrolidone, *J. Mater. Chem.*, 2011, **21**(10), 3371–3377.

50 S. Stankovich, R. D. Piner, S. T. Nguyen and R. S. Ruoff, Synthesis and exfoliation of isocyanate-treated graphene oxide nanoplatelets, *Carbon*, 2006, **44**, 3342–3347.

51 N. Dien Kha Tu, J. Choi, C. R. Park, *et al.*, Remarkable Conversion Between n- and p-Type Reduced Graphene Oxide on Varying the Thermal Annealing Temperature, *Chem. Mater.*, 2015, **27**, 151020100206002.

52 U. Martinez, J. H. Dumont, E. F. Holby, *et al.*, Critical role of intercalated water for electrocatalytically active nitrogen-doped graphitic systems, *Sci. Adv.*, 2016, **2**, e1501178.